

RESEARCH ARTICLE

10.1029/2017JC013463

Scaling Analysis of Multipulsed Turbidity Current Evolution With Application to Turbidite Interpretation

Viet Luan Ho¹ , Robert M. Dorrell² , Gareth M. Keevil¹, Alan D. Burns³, and William D. McCaffrey¹

¹School of Earth and Environment, University of Leeds, Leeds, UK, ²Faculty of Science and Engineering, University of Hull, Hull, UK, ³School of Chemical and Process Engineering, University of Leeds, Leeds, UK

Key Points:

- A pulse merging phenomenon was observed in experimental multipulsed saline density currents over a wide range of initial conditions
- Merging lengths in prototype environments can be estimated based on a scaling analysis calibrated to experimental multipulsed flow data
- The mathematical model is applicable for turbidity currents generated by short, sequential breaches

Supporting Information:

- Table S1

Correspondence to:

V. L. Ho,
eevlh@leeds.ac.uk

Citation:

Ho, V. L., Dorrell, R. M., Keevil, G. M., Burns, A. D., & McCaffrey, W. D. (2018). Scaling analysis of multipulsed turbidity current evolution with application to turbidite interpretation. *Journal of Geophysical Research: Oceans*, 123, 3668–3684. <https://doi.org/10.1029/2017JC013463>

Received 15 SEP 2017

Accepted 8 APR 2018

Accepted article online 19 APR 2018

Published online 22 MAY 2018

Abstract Deposits of submarine turbidity currents, turbidites, commonly exhibit upward-fining grain size profiles reflecting deposition under waning flow conditions. However, more complex grading patterns such as multiple cycles of inverse-to-normal grading are also seen and interpreted as recording deposition under cycles of waxing and waning flow. Such flows are termed multipulsed turbidity currents, and their deposits pulsed or multipulsed turbidites. Pulsing may arise at flow initiation, or following downstream flow combination. Prior work has shown that individual pulses within multipulsed flows are advected forward and merge, such that complex longitudinal velocity profiles eventually become monotonically varying, although transition length scales in natural settings could not be predicted. Here we detail the first high frequency spatial (vertical, streamwise) and temporal measurements of flow velocity and density distribution in multipulsed gravity current experiments. The data support both a process explanation of pulse merging and a phase-space analysis of transition length scales; in prototype systems, the point of merging corresponds to the transition in any deposit from multipulsed to normally graded turbidites. The scaling analysis is limited to quasi-horizontal natural settings in which multipulsed flows are generated by sequences of relatively short sediment failures (<10 km long) that develop progressively up-dip and predicts pulse merging after only a few tens of kilometers. The model cannot provide quantitative estimation of merging in down-slope flows generated by axially extensive (>10 km) sequences of breaches or where pulsing arises from combination at confluences of single-pulsed flows, such flows may be responsible for the pulsing signatures seen in some distal turbidites, >100 km from source.

1. Introduction

Turbidity currents are a form of dilute sediment-bearing gravity flows and play a key role in the transportation of clastic sediments from continents to deep seas (Carter et al., 2012; Hughes Clarke et al., 2012; Palanques et al., 2006; Piper & Savoye, 1993; Simpson, 1982; Xu et al., 2004). Such currents are driven by gravitational force resulting from the suspension of sediments within the interstitial fluid (Huppert, 1998; Kneller & Buckee, 2000; Middleton, 1993; Sequeiros, 2012).

Sediments deposited from turbidity currents, turbidites, build some of the largest sedimentary landforms on the planet (Canals et al., 2004; Lintern et al., 2016; Xu, 2011). Vertical grading patterns of deposits from individual turbidity current events reflect overpassing flow dynamics (Goldfinger et al., 2012; Hand, 1997; Ho et al., 2018; Kneller & McCaffrey, 2003; Stevenson et al., 2013). With the assumption that sediments aggrade progressively from overpassing flows, normally graded turbidites are deposited by flows with an abrupt waxing and a progressively waning velocity structure (Bouma, 1962). In the initial waxing flow regime, the current is weakly depositional; thus the basal layer comprises only a thin, or no, record of inverse grading (Hand, 1997). However, vertical grain size profiles of some turbidites are much more complex, with single deposits exhibiting multiple intervals of inverse-to-normal graded sediment. These deposits are referred to as pulsed or multipulsed turbidites (i.e., Goldfinger et al., 2012; Ho et al., 2018).

Many seismically triggered turbidites, generated at active tectonic margins, exhibit this complex vertical grading pattern (Gutiérrez-Pastor et al., 2013; Sumner et al., 2013). These turbidites are interpreted as being formed by multipulsed turbidity currents with repeated waxing-waning velocity structure (i.e., Ho et al., 2018; Kneller & McCaffrey, 2003). Repeat pulses in turbidity currents can be generated by: (i) retrogressive slope failures initiated by pulsed earthquakes whose magnitudes of seismic shaking may vary over time, or

autogenically generated (Beeson et al., 2017; Goldfinger et al., 2012); (ii) shock/aftershock events (Johnson et al., 2017); (iii) due to the combination of multiple single flows at confluences (Ismail et al., 2016; Nakajima & Kanai, 2000); or (iv) variation in discharge of hyperpycnal fed turbidity currents (Mulder & Alexander, 2001). Delay times between different seismically generated pulses can range from minutes to hours (see, e.g., Hsu et al., 2008; Lupi & Miller, 2014).

Ho et al. (2018) conducted laboratory experiments to model pulsing in denser-than-ambient gravity currents. At laboratory scale, saline flows were used as a proxy for turbidity currents driven by the suspension of fine-grained, low-settling velocity particulate material (Felix, 2002; Ferrer-Boix et al., 2015; Meiburg & Kneller, 2010). Results from these experiments indicate that individual pulse components within a multipulsed flow inevitably merge at some distance from source, and that the longitudinal velocity structure of the flow transforms from being cyclically varying to monotonically varying with increasing time and space (Ho et al., 2018). Therefore, up to the point of merging multiple coarsening-upward intervals might be expressed in the deposit, whose spatial separation might progressively reduce up to that point. Downstream of the merging point, deposits should be normally graded.

Here we advance the analysis of Ho et al. (2018), to assess the scaling between multipulsed gravity current experiments and prototype environments. Such analysis is essential to assess whether the merging phenomenon should be expressed in the geological record, and if so, over what range of scales. An extensive series of lock-exchange saline flow experiments was conducted to study a complete phase space of boundary conditions, from which a robust scaling analysis was developed. This enables the first empirically grounded test of the natural scale of the merging phenomenon to be undertaken. This paper presents (i) experimental data detailing the dynamical variations of single-pulsed flows and multipulsed flows, (ii) numerical analysis of the interdependence between nondimensional parameters characterizing initial flow conditions and the merging phenomenon, (iii) discussion regarding reasonable timescales over which the generation of multipulsed flows could be possible, and (iv) examples of natural turbidite interpretations in which the analysis effectively provides a tool to estimate the spatial persistence of pulsed turbidites.

2. Methodology

Experiments were run in order to: (i) confirm that pulses within multipulsed flows eventually merge (across the range of boundary conditions considered) and (ii) establish a scaling analysis that links experimental and real-world merging scales.

2.1. Experimental Setup

Experimental gravity currents were developed from the lock-exchange release of a denser-than-ambient (saline water) fluid into an ambient (tap water) (see, e.g., Holyer & Huppert, 1980; Middleton, 1966). Denser-than-ambient saline flows were experimentally modeled in a 5 m long flume with two lock boxes set up at one end which enabled the generation of multiple flow pulses in series (Figure 1a), based upon the method of Ho et al. (2018). The dynamics of saline flows approximate the dynamics of fine-grain dominated turbidity currents (see, i.e., Hogg et al., 2016; Islam & Imran, 2010; Kneller & Buckee, 2000). The speed of the lock gate lift was set by a pneumatic ram at 1.0 m/s in order to minimize turbulent mixing caused by the withdraw. The timing between each gate was set by an electronic timer, ensuring experiment repeatability. Effects of returning waves upon the slumping of dense fluid in the lock boxes were minimized by deploying two overspill boxes, one at each end of the flume. Two flow pulses were dyed yellow and blue to enhance the visualization and recorded using two cameras which could be independently moved laterally in front of the flume; each camera tracked one flow component. In order to study dynamical variations of single-pulsed and multipulsed flows in details, time series streamwise velocity and density data were collected for three characteristic flows of 0.125 m lock length. Furthermore, to underpin a scaling analysis of flow merging phenomenon, a series of experiments was conducted that confirmed individual pulses in multipulsed flows eventually merge over a wider range of conditions (see section 2.2).

Single-pulsed (0 s delay time), short and long delay time multipulsed flows were modeled. Such flows of three different delay times between pulses are thought to act as proxies for natural full-scale counterparts whose delay times can range between zero and several hours (see, e.g., Goldfinger et al., 2017; Hsu et al., 2008; Lupi & Miller, 2014). Single-pulse flows were initiated by the instantaneous release of both lockboxes.

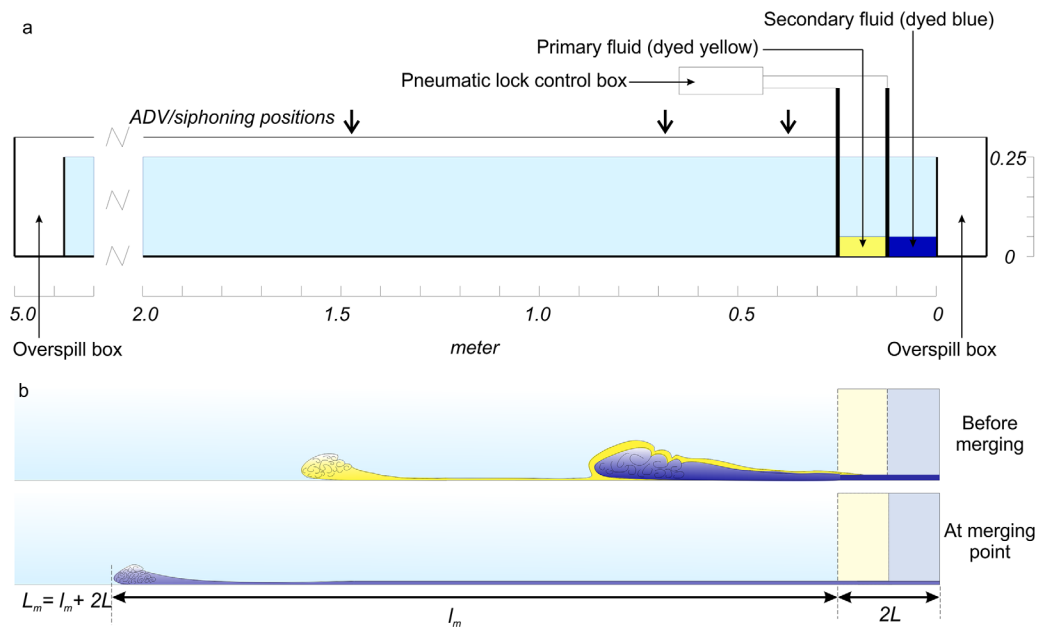


Figure 1. (a) Sketch of experimental setup (adapted from Ho et al., 2018). Note: (i) Three arrows sketched along the top of the flume indicate positions of Acoustic Doppler Velocimetry/siphoning instrumentation, (ii) two cameras were set up on a track fixed in front of the flume, (iii) initial flow height $h = 0.05$ m (see vertical scale bar). (b) Flow propagation model with lock length, L , merging length, l_m , and total merging length, L_m , highlighted.

Short delay time flows were those in which fluid contained in the second lockbox was released when the ratio between the height of that in the first lockbox and the original height had decreased to between 0.5 and 0.25. In long delay time flows, a second pulse was released after the dense fluid in the first lockbox had already fully collapsed and at that point the first pulse had traveled to a distance of ~ 11 lock lengths. Excess density, ambient height, and flow depth in all experiments were kept at 5% (fluid density $1,050 \text{ kg m}^{-3}$), 0.25 and 0.05 m, respectively, in order to maintain a turbulent flow condition ($Re \sim 4,000$). The ratio of initial flow depth/ambient was 0.2 which approximates to real-world scale of ca. 0.13 in deep marine turbidity currents (Piper et al., 1988; Talling et al., 2013; Xu et al., 2014).

Velocity and density sampling were undertaken for three characteristic short lock length flows of $L = 0.125$ m, $H = 0.25$ m, $h = 0.05$ m and $\Delta t = 0, 4$, and 15 s. These three delay time settings characterize single-pulsed, short and long delay time flows, respectively. Acoustic Doppler Velocimetry (ADV) was used to capture vertical variations in horizontal velocity (Brand et al., 2016; Craig et al., 2011; MacVicar et al., 2014; Thomas et al., 2017). The ADV probe was set at 7.1 cm above the flume bed, capturing a flow depth of 2.5 cm. Both the saline and ambient were seeded with $10 \mu\text{m}$ hollow glass spheres to generate acoustic reflection. A siphoning technique was adopted to collect samples of flow fluids, using a multichannel peristaltic pump connected to an array of seven 2 mm diameter siphoning tubes, centered at 5 mm intervals to collect data from 0.5 to 4 cm above the channel bed. Samples were collected every 2 s over a period of 20 s and contained in an array of sample trays. The conductivity and temperature of each sample were measured using a Mettler-Toledo InLab 752-6 mm conductivity probe (Mettler-Toledo, 2017). The measurements were then used to calculate excess density based on standard algorithms for brine (see, e.g., Janz & Singer, 1975; UNESCO, 1983). Experimental data were acquired at three locations: (i) proximally to source (0.365 m), (ii) relatively proximally (0.675 m) to the point of merging, and (iii) distally from source (1.465 m) (Figure 1).

2.2. Scaling Analysis

2.2.1. Experimental Parameters

The scale dependency of flow merging on initial flow conditions is tested by varying experimental parameters. The only physical parameters that characterize the experimental multipulsed flows are: initial flow height (h), ambient height (H), lock length (L), reduced gravity of dense fluid (g'), delay time (Δt), kinematic viscosity (ν), and merging length (L_m), see Table 1. The total merging length L_m is given by the sum of the

Table 1
Experimental Parameters Conducted to Underpin a Scaling Analysis

Parameter	Value		
Lockbox length, L	0.125 m	0.25 m	0.375 m
Lock release delay time, ΔT	1–34 s	1–67 s	7–107 s
Gravitational buoyancy, g'	0.4905 m/s ²		
Ambient height, H	0.10, 0.125, 0.167, 0.25 m		
Initial flow height, h	0.05 m		

experiment, a number of selected experiments were repeated so that relative errors in their resultant merging lengths were assessed (see Table 3); mean relative error was then calculated to confirm the repeatability of experiments. Specifically, experiments of the same initial settings were run several times to see how merging lengths vary. In total 79, experiments were conducted.

The height of the flow exiting the lockbox was proportional to h . From this, a velocity scale of the gravity current head is given by a Froude number condition (Huppert & Simpson, 1980)

$$U = \sqrt{g'h} \quad (1)$$

The dimensionless ratio between inertial, Uh , and viscous forces, ν , (i.e., the Reynolds number) was $Re=4,000$. Thus, the flows were assumed to be fully turbulent and viscous affects were considered negligible.

In order to link the scales of experimental parameters to those of prototype environments, a nondimensional approach was deployed to model experimental data by using Buckingham Pi theory. The principle of the theory is that an equation describing a physical system in terms of n -dimensional parameters can be expressed by an equation of $n-k$ parameters, where k denotes the number of unique physical dimensions involved (e.g., Buckingham, 1914; Miragliotta, 2011). Here it is argued that the merging length, L_m , over which individual pulses in multipulsed gravity currents combine, must be an unknown function of the original six unknown variables

$$L_m = f(L, h, H, g', \nu, \Delta t) \quad (2)$$

By assuming viscous effects are negligible, equation (2) can be reduced to a relationship between four dimensionless groupings, including: the merging length scale ($\Pi_4 = \frac{L_m}{L}$); the flow buoyancy scale ($\Pi_1 = \frac{\sqrt{g'h}}{L/\Delta t}$); the initial flow aspect ratio ($\Pi_2 = \frac{h}{L}$); and the lockbox aspect ratio ($\Pi_3 = \frac{H}{L}$). The merging length scale is defined as the ratio between the experimentally observed merging length in each experiment, measured from the front of the first lockbox to the point of merging, and one lock length used in that experiment, see Figure 1b. Translating this to the real world, the merging length scale describes the magnitude of merging length relative to the initial dimension of the corresponding slumping breach. Total merging length is then defined by equation (2). The buoyancy scale describes flow velocity, equation (1), normalized by the velocity scale necessary for a flow to translate one lock length during the delay time Δt . The two other ratios define the scales of the flow itself and of the ambient, relatively to the lock length. The principal goal of this scaling

analysis is to seek a mathematical correlation—function F , based on numerical analysis, which describes the dimensionless merging length (Π_4) as a function of other dimensionless parameters (see equation (3) and Table 2)

$$\Pi_4 = F(\Pi_1, \Pi_2, \Pi_3) \quad (3)$$

2.2.2. Data Fitting

When varying initial flow parameters (see Tables 1 and 2) the evolution of multipulsed flow fronts, and thus the merging lengths, varied significantly (Figure 2). In Figure 2, for flows of the same lock length (denoted by symbols) and ambient height (shown in each plot), pulses were seen to merge at further distances as delay times between the two lock gates increased. However, a simple correlation

Table 2
Dimensionless Parameter Groupings

Dimensionless group	Experimental values
Buoyancy scale, $\Pi_1 = \sqrt{g'h}/\frac{L}{\Delta t}$	Varied between 0 and 45
Flow aspect ratio, $\Pi_2 = h/L$	0.13, 0.20, 0.40
Lockbox aspect ratio, $\Pi_3 = H/L$	0.27, 0.33, 0.4, 0.5, 0.67, 0.8, 1, 1.3, 2
Merging length scale, $\Pi_4 = L_m/L$	Collected from experiments

Table 3
Repeated Experiments and Error Analysis

Lockbox length (m)	Flow height (m)	Ambient height (m)	Nominal delay time (s)	Actual delay time (s)	Total merging length (m)	Relative error of delay time (%)	Relative error of merging length (%)
0.125	0.05	0.167	1.5	1.25 1.6	0.911 1.084	16.7 6.67	8.68 8.68
0.125	0.05	0.25	0.5	0.38 0.67	0.807 0.777	24 34	1.88 1.88
0.125	0.05	0.25	4	4.1 4 4 4	1.297 1.300 1.295 1.305	2.5 0 0 0	0.18 0.06 0.33 0.44
0.125	0.05	0.25	11.5	11.1 11.4	1.713 1.708	3.48 0.87	0.14 0.14
0.125	0.05	0.25	22.5	22.3 22.2	2.069 1.975	0.89 1.33	2.33 2.33
0.125	0.05	0.25	34	33.5 34	2.094 2.198	1.47 0	2.42 2.42
0.375	0.05	0.125	16	15.5 16.7	3.024 3.317	3.13 4.38	4.61 4.61
Mean						6.21	2.57
Standard deviation						9.65	2.72

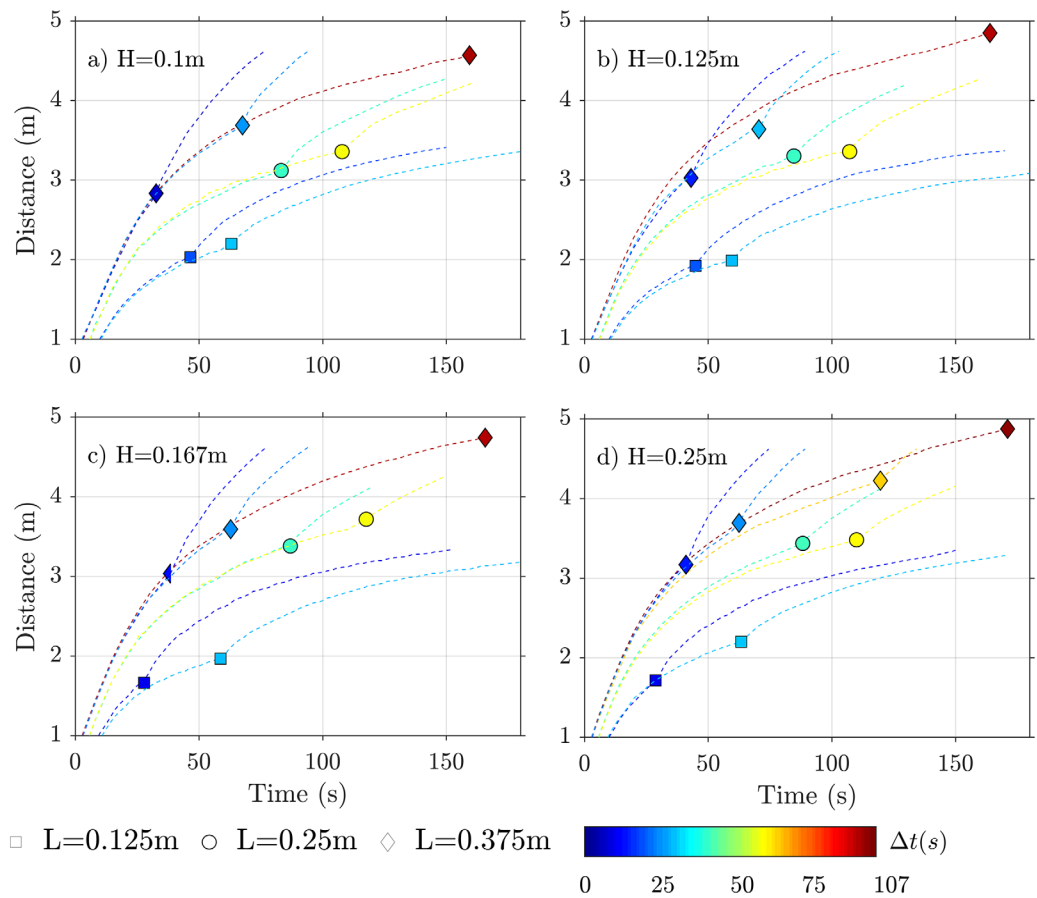


Figure 2. Front positions of some flows plotted based on different ambient heights (a) 0.1 m, (b) 0.125 m, (c) 0.167 m, and (d) 0.25 m. Note: Symbols on plots highlight points of merging in each experiment.

between merging lengths and any of the initial parameters is not directly observed from the raw data; it is not possible to simply visualize the variation of the data set comprising four varying parameters. Neither experimental repeatability (variability in merging length) nor the reliability of the experimental setup (variability in actual lock release delay times) can be implicated in the absence of simple correlations; relative errors of merging lengths observed in repeated experiments were insignificant (average 2.7%) and mean relative error in lock release delay times was small (average 6.21%), see Table 3. In the absence of a simple correlation between the merging length and initial parameters, a numerical regression of the dimensionless merging length scale with respect to the dimensionless parameters characterizing initial flow conditions was conducted.

The principal goal of the analysis is to test the interdependence of all parameters. Here a log-scale transform of the data was employed

$$P_{ij} = \log(\Pi_{ij}) \text{ for } i=1 \text{ to } 4 \text{ and } j=1 \text{ to } J=79 \quad (4)$$

to account for the possibility of nonlinear relationships between dimensionless parameters. This enabled linear regression analysis of the log-transformed data, of the form

$$P_{4j} = aP_{1j} + bP_{2j} + cP_{3j} + d \quad (5)$$

to be conducted; where a , b , c , and d are the coefficients to be determined. A least squares method was used to minimize the vector

$$\delta_j(a, b, c, d) = (aP_{1j} + bP_{2j} + cP_{3j} + d) - P_{4j} \quad (6)$$

containing the log-transformed experimental data, P_{ij} , collected from all $J=79$ experiments. Here the function δ_j describes the differences between numerically estimated (first term on the left-hand side of equation (6)) and experimentally observed (second term on the left-hand side of equation (6)) log-transformed dimensionless merging lengths. MATLABTM numerical nonlinear data-fitting solver, *lsqnonlin*, was used to find the optimal solution of (5) by simultaneously varying a , b , c , and d to find the global minima across all experiments conducted, defined by A , B , C , and D

$$\min\left(\sum_{j=1}^J \delta_j(a, b, c, d)^2\right) \equiv \sum_{j=1}^J \delta_j(A, B, C, D)^2 \quad (7)$$

A test of initial conditions revealed that numerical solutions were independent of the starting point chosen, suggesting a single global minimum of equation (6) (see further section 3.2). Starting points for the scalar variables $a-d$ in the numerical minimization of equation (6) were thus set to unity. During each iteration step, the solver simultaneously varied and updated the four variables, using result obtained from a preceding iteration until the minimum least squares error was found. Optimization, using the “*lsqnonlin*” solver, employed the Levenberg-Marquardt algorithm (see, i.e., Fan, 2003; Marquardt, 1963); the iteration process was terminated at a relative tolerance point of 10^{-6} . To evaluate the accuracy of the data fit, relative root mean square error (RMSE) was calculated by

$$\text{RMSE} = \sqrt{\frac{1}{J} \sum_{j=1}^J \left[\frac{AP_{1j} + BP_{2j} + CP_{3j} + D - P_{4j}}{P_{4j}} \right]^2} \quad (8)$$

3. Results

In this section, two components of experimental data are presented: (i) a detailed description of velocity and density data that, under the studied experimental configurations to model three characteristic flows (at $L=0.125$ m, $H=0.25$ m, $h=0.05$ m, and $\Delta t=0, 4$, and 15 s), show the inevitability of merging of pulses within multipulsed flows of different delay times and (ii) a scaling analysis to quantitatively model such phenomenon based upon a variety of initial boundary conditions.

3.1. Flow Dynamics

In this section, the dynamics of single-pulsed, short and long delay time flows are discussed by considering three examples of characteristic flows of short lock length (0.125 m) that were modeled.

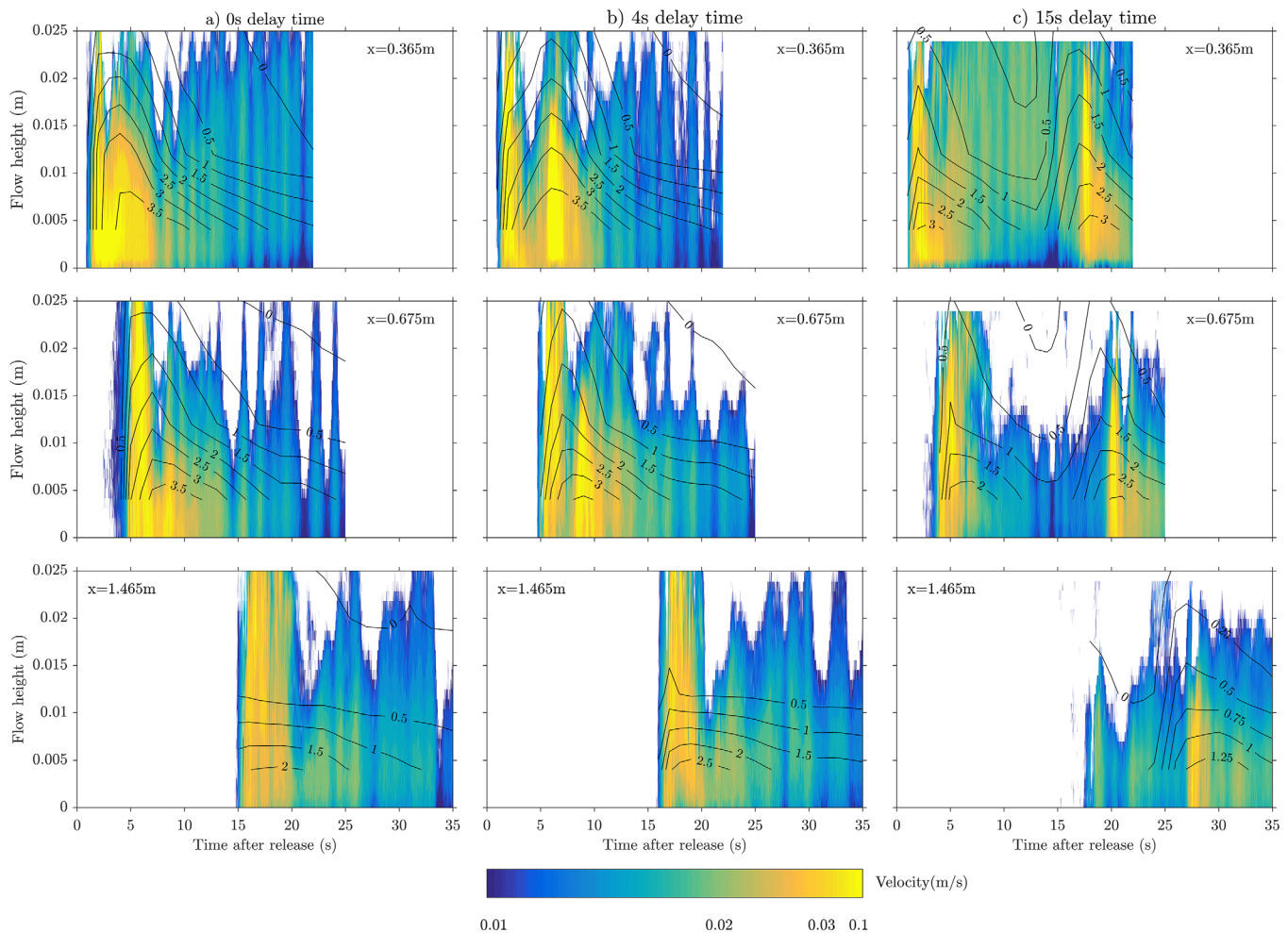


Figure 3. Time series velocity (contour fields) and density (contour curves) data collected from experiments of (a) single-pulsed flow, (b) short delay flow, and (c) long delay flow, in which $L=0.125$ m, $H=0.25$ m, and $h=0.05$ m. Note: (i) Contour curves show excess density in percentage, (ii) vertical stripes indicate the effects of surface waves of small magnitude, and (iii) the x value shown on each plot indicates the position along the flume, where the ADV/siphoning data were taken.

3.1.1. Single-Pulsed Flow

In single-pulsed flow experiments, the two flow pulses were released simultaneously. The total volume of fluid released was the same as in equivalent size and density as the multipulsed flows, but only a single front developed. The flows exhibited the waxing-waning velocity structure commonly observed in other experimental and field-based studies (Figure 3a; Britter & Simpson, 1978; Ho et al., 2018). The velocity maximum of the flow was located at approximately 25% of the flow height above the channel bed as has been observed in previous experimental and field-based research (Kneller & Buckee, 2000; Talling et al., 2015).

Time series density profiles at three downstream positions show that the flow head was always denser than the body. The turbulent mixing between flow and the ambient was more pronounced at the back of the head (Figure 3a; Sher & Woods, 2015), consistent with the net forward advection of material into the head from the body (Kneller et al., 1999). This process resulted in the reduction in density of the fluid comprising the flows, which is shown by the considerable change in vertical gradient in fluid density within the first 10 s of each sampling period in Figure 3a. Within the slumping phase, turbulent mixing and ambient entrainment appeared significant (Figure 3a, 0.365 m). As the flow traveled further downstream, it entrained more ambient fluid and thus flow density was generally reduced (Figure 3a at 0.675 and 1.465 m).

3.1.2. Short Delay Time Flow

Proximally to source, short delay time flows exhibited two separate pulses in velocity profiles; the second pulse traveled faster than the first one (Figure 3b, 0.365 m). As the second pulse was progressively advected

toward the flow front, the temporal separation between two pulses was progressively reduced and the magnitudes of internal fluid velocity of two pulses became relatively comparable (Figure 3b, 0.675 m). Once the two pulses merged completely, the flow evolved in a manner similar to that of the single-pulsed flow (Figures 3a and 3b, 1.465 m). The velocity maximum was also located at $\sim 25\%$ of flow height as seen in single-pulsed flow's velocity profile (Figure 3b).

The advection of the second pulse as an intrusion (Ho et al., 2018) within the first pulse is shown by an increase in flow density observed after the arrival of the flow front at the siphoning probe (Figure 3b, 0.365 m, 5–10 s). As the second pulse progressively intruded into the first pulse, two pulses progressively merged and the density profile observed is very similar to that of single-pulsed flow at the same sampling position along the channel pathway (Figures 3a and 3b, 0.675 m). The density of the second pulse was better preserved in comparison to that of the first pulse, presumably since it traveled as an intrusion into a denser-than-water ambient. As a result, the short delay time multipulsed flows exhibited a relatively thick basal layer of high density (Figure 3b, 1.465 m).

3.1.3. Long Delay Time Flow

Proximally to source, two pulses of the long delay time multipulsed flows each traveled at velocity of ca. 0.1 m/s (Figure 3c, 0.365 m). As the flow evolved further from source, the velocity of the first pulse decreased significantly while the second pulse maintained a relatively high velocity (Figure 3c, 0.675 and 1.465 m). Thus, the second pulse was progressively advected toward the flow front. This is demonstrated by the reduction in temporal separation between the pulses (Figure 3c). The ADV data show that two pulses eventually merge to form a unified flow.

Prior to the arrival of the second pulse at the sampling position, the first pulse developed a thin layer of high density (Figure 3c, 0.365 m, 0–10 s ca. 0.004 m of 3% excess density). Following the second pulse release, both pulses had relatively dense bases (i.e., excess density of approximately 3% shown in Figure 3c, 0.365 m). Further downstream from source, the dense fluid comprising the second pulse maintained a higher density than that comprising the first pulse (i.e., Figure 3c, 0.675 m, excess density 3% versus 2%), while the first pulse was significantly diluted because of ambient entrainment. The whole flow generally became diluted with increasing time and space (Figure 3c). Time series density data also show the two pulses progressively merging as their temporal separation was progressively reduced (Figure 3c).

3.2. Scaling Analysis

By numerically solving equation (6), a line of best fit is determined that provides the best collapse of the dimensionless experimental data, where $A=0.28$, $B=0.21$, $C=0.04$, and $D=0.75$. By inverting the log-transform of equation (5), an equation is found for the merging length scale, l_m ,

$$\frac{l_m}{L} = 10^{0.75} \left[\frac{\sqrt{g'h}}{L/\Delta t} \right]^{0.28} \left[\frac{h}{L} \right]^{0.21} \left[\frac{H}{L} \right]^{0.04} \quad (9)$$

The associated RMSE for this data collapse is 6.8% (see Figure 4). However, for the dimensionless flow aspect ratios considered, equation (8) only has a weak dependence on the lockbox aspect ratio Π_3 . This motivates development of a model of the merging length scale of reduced complexity that is independent of the ambient flow depth. To test this hypothesis of reduced complexity, a correlation was sought that was independent of H/L . The same minimization approach, based on least squared method, was used on the function

$$\delta_j(a, b, d) = aP_{1j} + bP_{2j} + d - P_{4j} \quad (10)$$

see equations (4–8), section 2.3.2. The optimal simplified scaling of the merging length incorporates only three dimensionless parameters, the lock box length, reduced buoyancy, and delay time,

$$\frac{l_m}{L} = 10^{0.70} \left[\frac{\sqrt{g'h}}{L/\Delta t} \right]^{0.25} \left[\frac{h}{L} \right]^{0.25} \quad (11)$$

and its RMSE showing the deviation between experimentally observed and theoretically estimated merging lengths is approximately 7% (Figure 5). The difference between RMSE of the original and simplified data collapses, equations (9) and (11), is insignificant—only 0.2%. Further, data fitting is insensitive to local

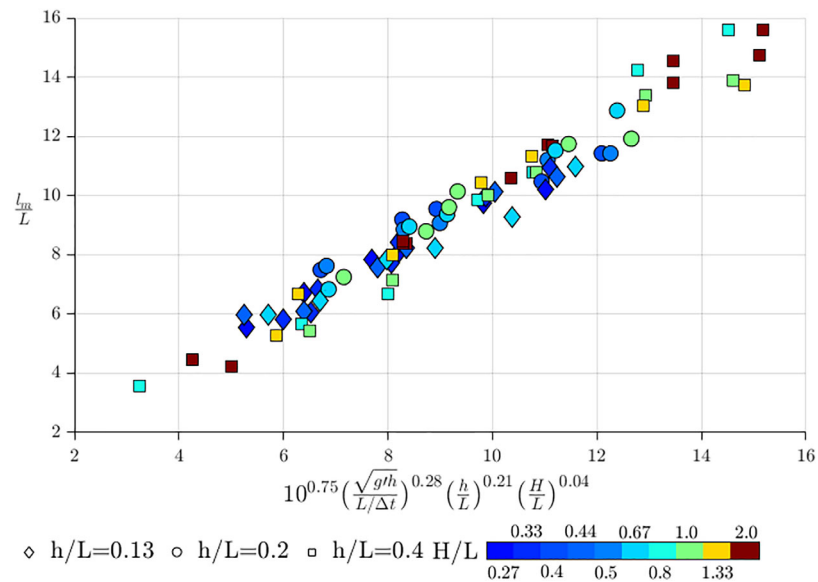


Figure 4. Data regression showing merging length as a linear function of initial dimensionless parameters, obtained using MATLAB™ numerical nonlinear data-fitting solver, *lsqnonlin*. Note: $R^2 = 0.96$, RMSE = 6.8%.

variations; for A and B between 0.2 and 0.4, the RMSE resulting from any data regression changes by only 5% (Figure 5). Figure 5 also shows the well-behaved character of the minimization function, equation (6), with a single global minimum in the domain $A, B \in [0 \dots 1]$.

This suggests that when the flow aspect ratio, h/L , is small the merging length scales are independent of the ambient depth. This may be because the hydrostatic pressure driving force of shallow partial release lockbox gravity currents is, similarly to turbidity currents, mainly controlled by the excess density between the flow and the surrounding ambient (see, i.e., Bonnecaze et al., 1993; Darby & Peakall, 2012; Shin et al., 2004).

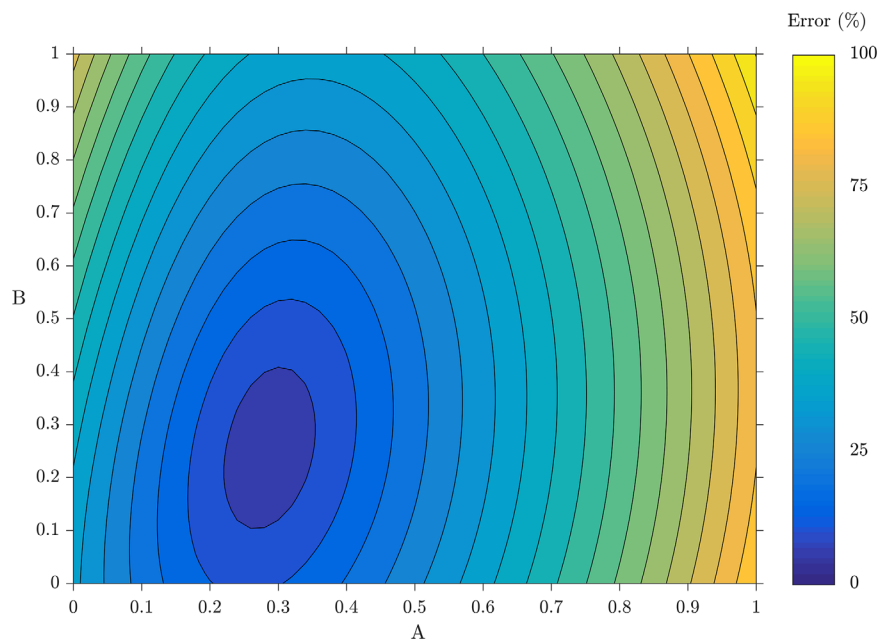


Figure 5. Contour plot showing variation of RMSE of different data fittings, equation (11), resulting from varying A and B within 0–1.

4. Discussion and Application

4.1. Merging Phenomenon

The variations in flow dynamics of both short and long delay time multipulsed flows show that the signature of the intrusion of a second pulse within a multipulsed flow is preserved proximally to source, progressively distorted toward the point of merging and eventually shredded once pulses completely merge (Figure 3; Ho et al., 2018). Multipulsed flows of both short and long delay time evolve from being repeatedly waxing-waning to monotonically waning. Therefore, beyond the point of merging, such multipulsed flows of both delay time settings evolve in a similar manner to that of single-pulsed flows of equivalent volumes of dense fluid.

The second pulse progressively intrudes into the first and they eventually merge. However, before reaching such merging points, the way in which the second pulse is advected differs between the short delay time flows and the long delay time flows. In multipulsed flows of short delay time, the first pulse quickly develops a density stratification because of ambient entrainment (i.e., Britter & Simpson, 1978; Hallworth et al., 1996) prior to the second pulse release. The vertical density profile of the first pulse's body commonly exhibits a thick basal layer of relatively high density (Figure 6a). The second pulse then intrudes into the first at a neutrally buoyant level, vertically modulated by the velocity field within the first pulse (i.e., Ho et al., 2018). Given that the maximum internal velocity of fluid within a turbidity current's body is always higher than the head velocity (Hughes, 2016; Kneller et al., 1999; Sher & Woods, 2015), the second pulse, once reaching the first pulse's body, will eventually be advected toward the flow front.

In multipulsed flows of long delay time, at the second gate time, the first pulse has already traveled a significant distance away from source (c. 11 lock lengths). The remnants of the primary flow near the lockbox consist of a very thin layer that has the density of the prerelease flow. Above this thin layer, there is a strongly stratified very dilute cloud, resulting principally from flow induced mixing with the ambient at the head (although such stratification might also be attributed to turbulent mixing caused by lock gate removal,

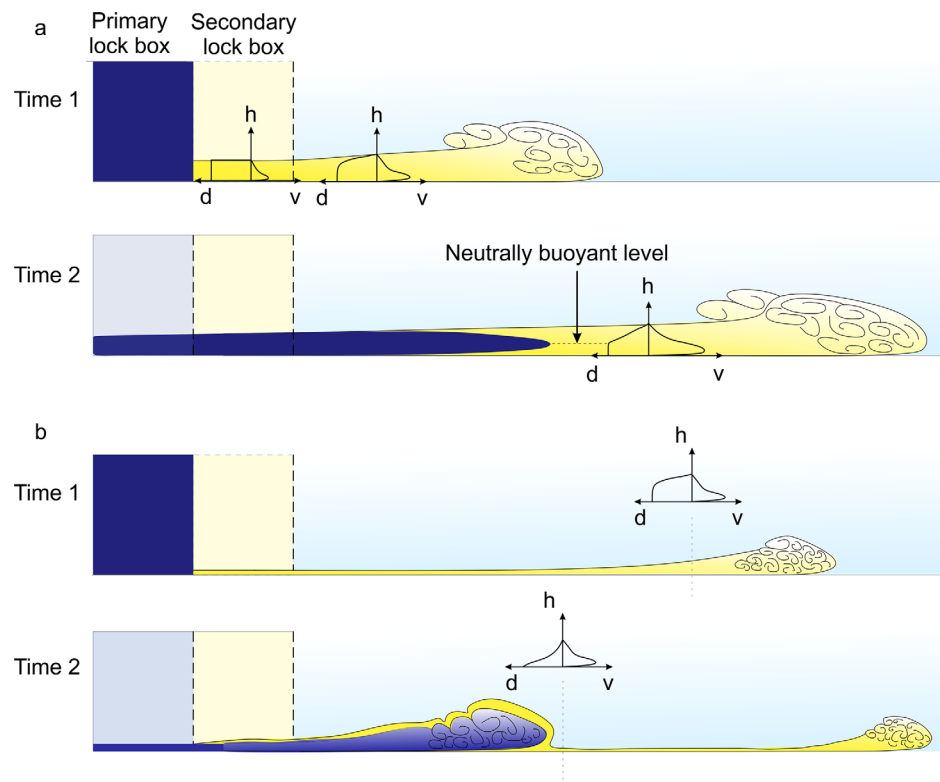


Figure 6. Conceptual models of the intrusion of the second pulse in (a) short delay time flows (adapted from Ho et al., 2018) and (b) long delay time flows. Note: In Figure 6b, (i) the nose of the secondary pulse is lifted off the bed and (ii) the dilute cloud remnant flow from the first pulse above the second pulse.

the speed of the lock gate release was set to minimize this effect). As the height of the dense layer is much smaller compared to that encountered in the short delay time flows, the second release of dense fluid will be located much closer to, or on, the bed. Here the second pulse front is much thicker than the thin layer remnants of the first pulse and is much denser than the background density of the cloud generated by the first flow, which has negligible effect on the flow. Therefore, the second pulse forms a bore traveling on top of the thin layer (of original flow density) of the first pulse. Thus, the remnants of the first pulse act as a lubricating layer reducing bottom boundary layer drag in the second pulse (see, e.g., Ho et al., 2018). By reducing drag, the second pulse travels faster than the first such that it is eventually advected toward the front of the flow, where internal velocity gradients control pulse merging (Figure 6b). However, this process will take comparatively longer than the intrusion process in shorter delay flows as the near lock gate velocity field of the first pulse is negligible and thus has little effect on the advection of the second pulse.

The variations in longitudinal velocity structure of multipulsed flows should be expressed in any associated turbidites such that the deposits exhibit a progressive spatial transition in grading pattern along the flow pathway from multipulsed to single-pulsed. Thus, multipulsed turbidites are expected to be deposited proximally and unipulsed deposits distally. The vertical separation between multiple intervals of coarse grain size within any multipulsed turbidite units should progressively reduce as a consequence of reduced temporal separation between flow pulses with increasing time and space. Beyond the point of merging, unipulsed turbidites with a monotonic upward-fining grading pattern should be deposited. Thus, no inference regarding flow initiation mechanisms should be made based on the grading patterns of distal turbidites (Ho et al., 2018).

4.2. Application of the Scaling Analysis

Assuming that the dynamics of real-world submarine flows can be approximated by saline lock-exchange flows studied in the laboratory (Ho et al., 2018), equations (9) or (11) can be used to predict the natural merging lengths of channelized 2D flows; further, they may provide qualitative insight into merging in flows that are free to expand laterally. For simplicity, using the reduced form, equation (11), the key parameters to predict merging lengths are: the flow height (h), initial breach length (L), reduced gravity of dense fluid (g') (or flow concentration, see Table 4 for relationship between the two parameters), and delay time (Δt). Initial axial breach length and delay time are two independent variables. Here variations and correlations of flow height and concentration are based on data from natural flow events (see supporting information). The flow height and concentration data were collected directly from the literature (see Best et al., 2005; Chikita, 1990; Chikita & Okumura, 1990; Cooper et al., 2013; De Cesare et al., 2006; Gilbert et al., 2006; Gutscher et al., 2006; Johnson & Satake, 1994; Lambert & Giovanoli, 1988; Liu et al., 2012; Mikada et al., 2006; Pharo & Carmack, 1979; Nelson et al., 2015; Talling et al., 2013; Umeda et al., 2006; Vangriesheim et al., 2009; Xu, 2010; Xu et al., 2010); some concentration measurements were estimated using the frictional-gravitational force balance model of Parker et al. (1987) (see, e.g., Abad et al., 2011)

$$S = \frac{C_f + e_w(1 + 0.5Fr^{-2})}{Fr^{-2}} \quad (12)$$

where S , C_f , e_w , and Fr are channel slope, bed friction coefficient, dimensionless coefficient of entrainment, and Froude number, respectively. Friction coefficient C_f was determined as $1/Cz^2$ in which Chezy resistance coefficient, Cz , equals 20 (see, e.g., Abad et al., 2011, Figure 24).

Table 4
Calculated Merging Lengths for Multiple Canyon Head Scale Failures

Parameters	Calculations
Initial flow height $h=200$ m $\rho_s=2,650$ kg/m ³ and $\rho_o=1,000$ kg/m ³ Flow concentration $c=0.0315$ Delay time $\Delta t=600$ s Initial breach length $L=3,000$ m	<ul style="list-style-type: none"> Reduced gravity: $g' = g \left(\frac{\rho_s - \rho_o}{\rho_o} \right) c = 0.051$ m/s² Normalized merging length: $\frac{l_m}{\sqrt{L}} = 10^{0.7} [\sqrt{g'h} \Delta t h]^{0.25} \sim 166.3$ m^{1/2} Merging length: $l_m=9,108$ m, $L_m=15,108$ m

Since flow height and concentration are interdependent (see, e.g., Abad et al., 2011), a conditional probabilistic distribution was derived from the empirical data. This enabled a correlation between flow height and concentration to be estimated (Figure 7). Rearranging equation (11), we find that a dimensional merging length parameter takes the form

$$\frac{l_m}{\sqrt{L}} = 10^{0.7} \left[\sqrt{g'h} \Delta t h \right]^{0.25} \quad (13)$$

i.e., merging lengths scale with the square root of initial release length scale. Based on the quantified domains of flow height and concentration (e.g., flow height and reduced gravity terms in equation (13)) shown in Figure 7, probability distribution and cumulative functions detailing the possibility of different values of $\frac{l_m}{\sqrt{L}}$ were determined using equation (13) at a fixed flow delay time (Figure 8).

An example calculation of merging length is laid out as follows. Assuming that initial flow height, concentration, and delay time between two pulses of a seismically triggered bipulsed turbidity currents are 200 m, 0.0315 and 10 min, respectively (see, e.g., Heezen & Ewing, 1952; Nelson et al., 2015; Piper et al., 1999), equation (13) yields a value of normalized merging length as $\sim 166.3 \text{ m}^{1/2}$ (see Table 3). Approximately 59% of the sampled data has normalized merging lengths lower than $166.3 \text{ m}^{1/2}$ (Figure 8). By assuming that the associated axial breach length is 3,000 m, generated for example by a canyon head failure (see, e.g., Dengler et al., 1984), the total merging length is calculated as 15,108 m. Hence, within $\sim 15 \text{ km}$ from the point of initiation, multipulsed turbidites are expected to be deposited, and beyond, unipulsed turbidites, from which no inference of the flow initiation mechanism could be made.

The short predicted merging lengths calculated on the assumption that canyon head failure is typically associated with relatively short breach lengths contrast with the apparently common occurrence of multipulsed turbidites in active tectonic margins at much more distal locations from the continental shelves where the depositing turbidity currents were initiated. For example, Gutiérrez-Pastor et al. (2013) discuss the

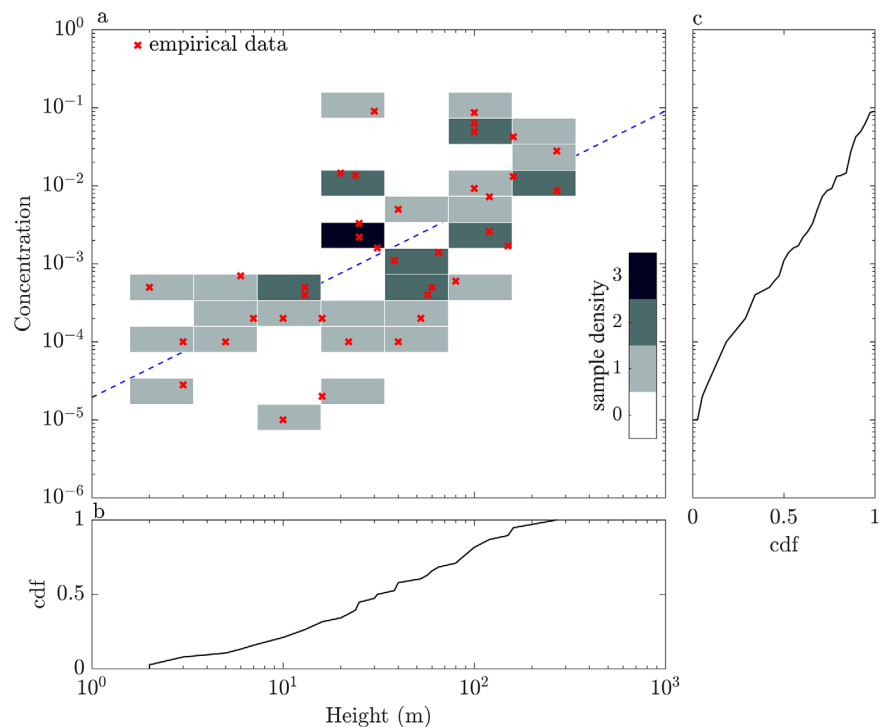


Figure 7. Probability distribution plots of recorded natural flow height and concentration (a) conditional density plot showing the density of co-occurrence of different flow heights and concentrations between the considered empirical data, (b) cumulative density function of flow height, and (c) cumulative density function of concentration. Note: (i) Different colors indicate numbers of occurrence of a flow height at a given concentration, (ii) red crosses indicate empirical values of flow height and concentration (data used in this plot are provided in the supporting document; see, e.g., Talling et al., 2013 and other cited references), and (iii) dashed line shows nonlinear correlation between flow height and concentration.

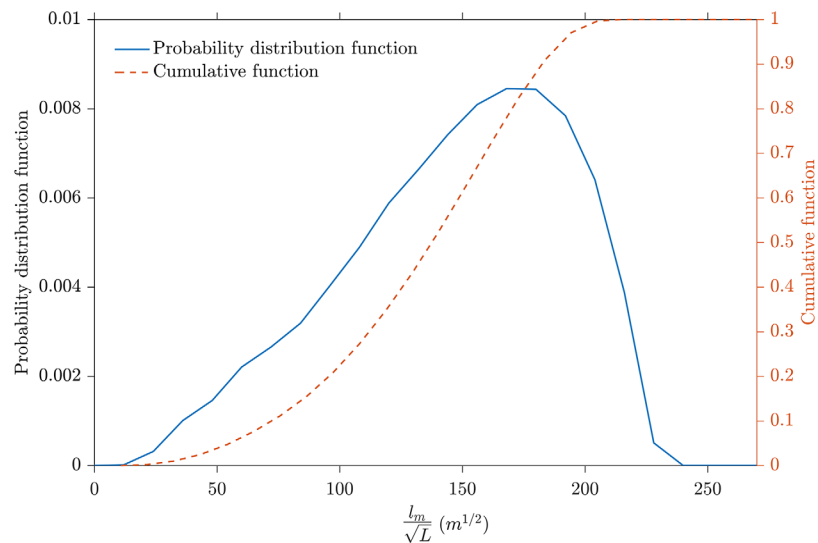


Figure 8. Probability distribution and cumulative functions of normalized merging lengths $\frac{l_m}{\sqrt{L}}$ computed at delay time $\Delta t = 10$ min.

presence of multipulsed turbidites in the Cascadia region at locations ranging from 100 to 1,000 km from channel heads. Therefore, the assumptions on initial flow conditions (i.e., flow height, concentration, breach length, and delay time), or the differences between experimental and real-world flow initiation mechanisms (e.g., sequential breaching (Goldfinger et al., 2012; Johnson et al., 2017) and confluence merging (Goldfinger et al., 2017)) used in the example calculation may not be plausible.

To test the sensitivity of the predicted merging length to the values of initial flow conditions a parametric analysis was conducted in which all but one of the assumed parameters shown in Table 4 were retained, and the other parameter varied. From equation (13) merging length can be seen to scale with reduced gravity to the power of one-eighth, initial flow height to the three-eighths, or initial axial length to the four-eighths (Figure 9). Therefore, initial axial length is the dominant control on the merging length. Varying the other three parameters within realistically broad domains does not change the merging length scale as significantly (Figures 9b–9d).

4.3. Initiation Mechanisms of Multipulsed Turbidity Currents

Multipulsed turbidity currents might be generated due to (i) retrogressive failures in which each slumping episode results in the formation of a pulse component or (ii) combination at downstream confluences of multiple single-pulsed flows sourced from upstream attributes. The delay time between individual flow components within a multipulsed flow is then controlled by (i) the temporal separation between sequential slumping episodes, shock/aftershock events (between minutes and hours; see, e.g., Heezen & Ewing, 1952; Piper et al., 1999) or (ii) travel time differences between single-pulsed flows generated in upstream confluences upon reaching such points.

Experiments conducted to support this scaling analysis were set up to model multipulsed flows generated by short, sequential, and discrete ruptures. The fluid contained in the second lockbox in each experiment was released after the backward-propagating wave of ambient fluid generated due to the collapse of the first release had reached the front of the second lock gate. In this way, the second release was always initially higher than the current generated by the first release, and propagated as a pulse into it. When lock release delay times are sufficiently short that the backward propagating wave has not traveled a distance of one lock length by the time of the second release, there is no difference in fluid levels across the lock gate at withdrawal. In this circumstance, the dynamics of the combined flow are essentially the same as those following release of a single, combined lock, such that a unipulsed flow will be generated.

The propagation distance of the backward wave determines whether staggered dambreak releases will behave as unipulsed versus multipulsed flows. The rearward propagating wave of a dambreak collapse has a velocity $dX(t)/dt = -\sqrt{g'h}$ (Shin et al., 2004), dependent on the reduced gravity and thus concentration

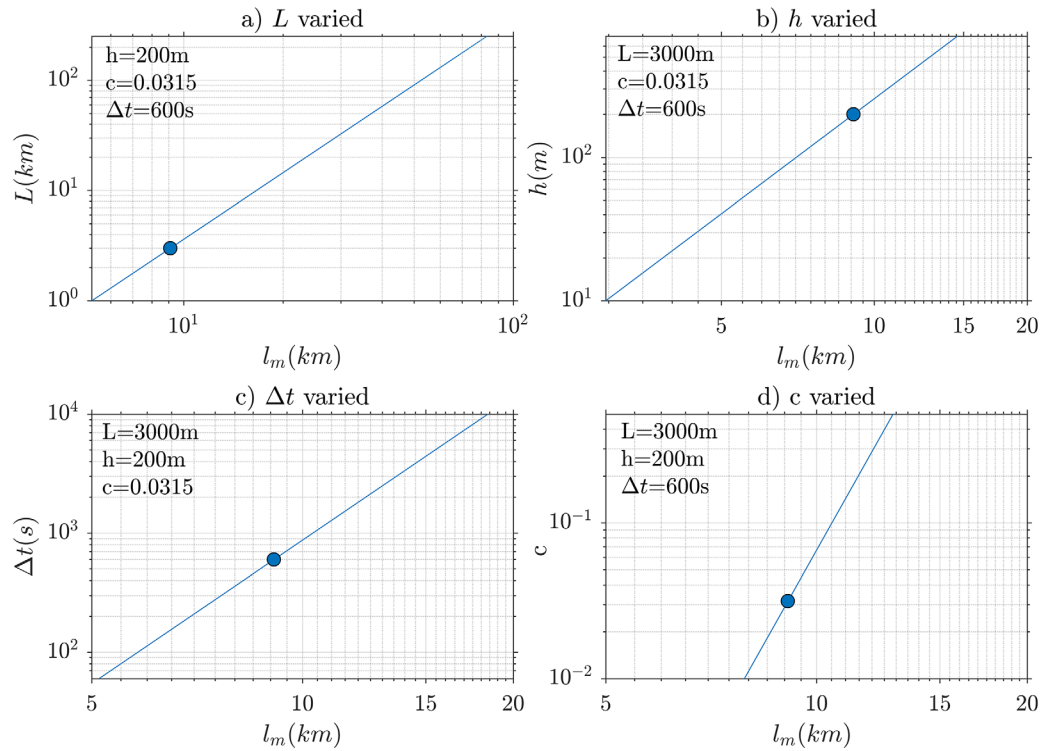


Figure 9. Parametric analysis of merging length scales on the variations of lock length, flow height, delay time, and concentration, equation (11), in which all but the selected parameter retained their values in Table 2, while the selected parameters were varied.

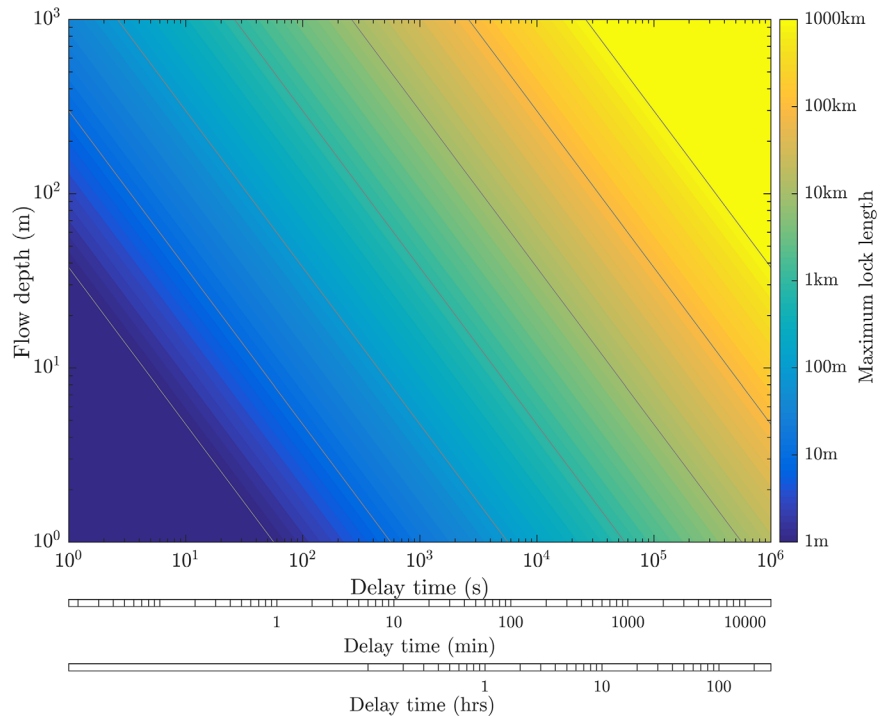


Figure 10. Diagram showing maximum lengths of lock that can produce a multipulsed gravity current for different combinations of flow height and delay time between successive releases (see text for discussion).

of the flow. A nonlinear correlation between flow height and concentration is derived from empirical data (Figure 7). The maximum wave travel distance (Figure 10) that can produce a multipulsed flow thus specifies the lock length (at laboratory scales) or breach length (at prototype scales). Given the value of initially constant flow height the wave travel distance at the delay time is $=\sqrt{g'h\Delta t}$.

In natural systems, the delay time might correspond to the interval between successive sediment failures that produce a multipulsed turbidite, or to the duration of a single triggering seismic event that directly generates a multipulsed turbidite (in the latter case, this duration may extend up to 10 min duration, see, e.g., Heezen & Ewing, 1952; Piper et al., 1999). Assuming a delay time of 10 min and a characteristic flow height of ca. 200 m, the maximum length of each individual breach that might produce a bipulsed current is 7.5 km (i.e., a combined breach length of 15 km). The scaling analysis predicts that such short breaches should be associated with relatively short merging lengths (e.g., 15.1 km in the example cited). It follows that multipulsed turbidites produced by single seismic events should be of relatively restricted extent and that, therefore, the model cannot account for the deposition of multipulsed turbidites observed at significant distances from continental shelves (see, e.g., Gutiérrez-Pastor et al., 2013).

It is worth bearing in mind, however, that the scaling model proposed carries the assumptions that flows propagate on a zero gradient channel and that they originally comprised two fluid components of identical volume. Natural multipulsed flows may initiate with flow components of different volume and will propagate down sloping pathways. The same differences apply to considerations of flow merging and associated pulse development in confluence settings, with the additional restriction that, on geometric grounds, the modeled height differences (i.e., a thicker intruding flow) are unlikely to be met, and that the mechanics of combination of separate flows may differ from the modeled scenario of juxtaposed axial releases. Such discrepancies between the simplified experimental model and natural setting warrant further exploration to assess whether the longer merging lengths documented in prototype settings (Goldfinger et al., 2017) might arise due to the effects of a more varied set of boundary conditions.

5. Conclusions

Data from experiments conducted to model saline multipulsed gravity currents in which initial boundary conditions were systematically varied reconfirm that multiple pulse components within a multipulsed flow must merge at some point from source provided the flows remain active. This observation implies that turbidity currents in natural settings represent one mechanism by which multipulsed turbidites can be deposited. Such deposits can persist up to the point where pulses merge; beyond that point normally graded turbidites should be deposited and no inference regarding flow initiation mechanisms is possible. An empirical scaling analysis (equations (9) and (11)) provides a tool to estimate the persistence of multipulsed turbidites in real-world environments, which suggests that initial axial breach is the key parameter that controls merging distances. Although the model can be used to predict merging distances in multipulsed turbidity currents generated due to retrogressive, discrete submarine failures of small scales (order of magnitude of less than 10 km), it cannot be directly applied to natural settings where initial breaches are extensive, on sloping flow pathways and where multipulsed flows are generated due to the combination of single-pulsed flows at downstream confluences. Multipulsed turbidites observed at extensive distances from continental shelves must have been deposited under the influence of a wider range of boundary conditions, including, but not restricted to development of flow pulses of nonequal volume, flow propagation pathways of significant slope and the combination of flows at confluences; the persistence of flow pulsing under such conditions is a topic that warrants further research.

References

- Abad, J. D., Sequeiros, O. E., Spinewine, B., Pirmez, C., García, M. H., & Parker, G. (2011). Secondary current of saline underflow in highly meandering channel: Experiments and theory. *Journal of Sedimentary Research*, *81*, 787–813.
- Beeson, J. W., Johnson, S. Y., Goldfinger, C., & Ross, A. F. (2017). The transtensional offshore portion of the northern San Andreas fault: Fault zone geometry, late Pleistocene to Holocene sediment deposition, shallow deformation patterns, and asymmetric basin growth. *Geosphere*, *13*, 1–34.
- Best, J. L., Kostaschuk, R. A., Peakall, J., Villard, P. V., & Franklin, M. (2005). Whole flow field dynamics and velocity pulsing within natural sediment-laden underflows. *Geology*, *33*, 765–768.
- Bonnecaze, R. T., Huppert, H. E., & Lister, J. R. (1993). Particle-driven gravity currents. *Journal of Fluid Mechanics*, *250*, 339–369.
- Bouma, A. H. (1962). *Sedimentology of some Flysch deposits: A graphic approach to facies interpretation* (168 p.). Amsterdam: Elsevier.

Acknowledgments

This work was funded by the Turbidites Research Group (TRG), sponsors: Anadarko, BP, ConocoPhillips, Dana Petroleum, ENI, HESS, Nexen, OMCV, Petronas, Shell, Statoil, Tullow, Woodside). None of the authors have any conflict of interest to declare. We would like to thank Robert Thomas and Helena Brown in the Sorby Environmental Fluid Dynamics Laboratory for their assistance with the experiments. Supporting information detailing flow heights, concentrations of natural flows and references are provided. We would also like to thank two reviewers whose comments and suggestions on an earlier version of this paper have helped improve this manuscript.

- Brand, A., Noss, C., Dinkel, C., & Holzner, M. (2016). High-resolution measurements of turbulent flow close to the sediment-water interface using a bistatic acoustic profiler. *Journal of Atmospheric and Oceanic Technology*, *33*, 769–788.
- Britter, R. E., & Simpson, J. E. (1978). Experiments on the dynamics of a gravity current head. *Journal of Fluid Mechanics*, *88*, 223–240.
- Buckingham, E. (1914). On physically similar systems: Illustrations of the use of dimensional equations. *Physical Review*, *4*, 345–376.
- Canals, M., Lastras, G., Urgeles, R., Casamor, J. L., Mienert, J., Cattaneo, A., et al. (2004). Slope failure dynamics and impacts from seafloor and shallow sub-seafloor geophysical data: Case studies from the COSTA project. *Marine Geology*, *213*, 9–72.
- Carter, L., Milliman, J. D., Talling, P. J., Gavey, R., & Wynn, R. B. (2012). Near-synchronous and delayed initiation of long run-out submarine sediment flows from record-breaking river flood, offshore Taiwan. *Geophysical Research Letters*, *39*, L12603. <https://doi.org/10.1029/2012GL051172>
- Chikita, K. (1990). Sedimentation by river-induced turbidity currents: Field measurements and interpretation. *Sedimentology*, *37*, 891–905.
- Chikita, K., & Okumura, Y. (1990). Dynamics of turbidity currents measured in Katsurazawa reservoir, Hokkaido, Japan. *Journal of Hydrology*, *117*, 323–338.
- Cooper, C., Wood, J., & Andrieux, A. (2013). *Turbidity current measurements in the Congo Canyon* (Paper presented at Offshore technology conference, 6–9 May, Houston, TX (12 p.)). <https://doi.org/10.4043/23992-MS>
- Craig, R. G. A., Loadman, C., Clement, B., Rusello, P. J., & Siegel, E. (2011). *Characterization and testing of a new bistatic profiling acoustic Doppler velocimeter: The Vectrino-II*. Paper presented at the IEEE/OES/CWTM tenth working conference on current measurement technology, Monterey, CA (pp. 246–252). <https://doi.org/10.1109/CWTM.2011.5759559>
- Darby, S. E., & Peakall, J. (2012). Modelling the equilibrium bed topography of submarine meanders that exhibit reversed secondary flows. *Geomorphology*, *163–164*, 99–109.
- De Cesare, G., Boillat, J.-L., & Schleiss, A. J. (2006). Circulation in stratified lakes due to flood-induced turbidity currents. *Journal of Environmental Engineering*, *132*, 1508–1517.
- Dengler, A. T., Wilde, P., Noda, E. K., & Normark, W. R. (1984). Turbidity currents generated by hurricane Iwa. *Geo-Marine Letters*, *4*, 5–11.
- Fan, J. (2003). A modified Levenberg-Marquardt Algorithm for singular system of nonlinear equation. *Journal of Computational Mathematics*, *21*, 625–636.
- Felix, M. (2002). Flow structure of turbidity currents. *Sedimentology*, *49*, 397–419.
- Ferrer-Boix, C., Martín-Vide, J. P., & Parker, G. (2015). Sorting of a sand-gravel mixture in a Gilbert-type delta. *Sedimentology*, *62*, 1446–1465.
- Gilbert, R., Crookshanks, S., Hodder, K. R., Spagnol, J., & Stull, R. B. (2006). The record of an extreme flood in the sediments of montane Lillooet lake, British Columbia: Implications for paleoenvironmental assessment. *Journal of Paleolimnology*, *35*, 737–745.
- Goldfinger, C., Galer, S., Beeson, J., Hamilton, T., Black, B., Romsos, C., et al. (2017). The importance of site selection, sediment supply, and hydrodynamics: A case study of submarine paleoseismology on the northern Cascadia margin, Washington USA. *Marine Geology*, *384*, 4–46.
- Goldfinger, C., Nelson, C. H., Morey, A. E., Johnson, J. E., Patton, J., Karabanov, E., et al. (2012). *Turbidite event history—Methods and implications for Holocene paleoseismicity of the Cascadia subduction zone* (U.S. Geol. Surv. Prof. Pap. 1661-F, 170p.). Reston, VA: United States Geological Survey. Retrieved from <http://pubs.usgs.gov/pp/pp1661f/>
- Gutiérrez-Pastor, J., Nelson, C. H., Goldfinger, C., & Escutia, C. (2013). Sedimentology of seismo-turbidites off the Cascadia and northern California active tectonic continental margins, northwest Pacific Ocean. *Marine Geology*, *336*, 99–119.
- Gutscher, M.-A., Baptista, M. A., & Miranda, J. M. (2006). The Gibraltar Arc seismogenic zone (part 2): Constraints on a shallow east dipping fault plane source for the 1755 Lisbon earthquake provided by tsunami modelling and seismic intensity. *Tectonophysics*, *426*, 153–166.
- Hallworth, M. A., Huppert, H. E., Phillips, J. C., & Sparks, R. S. J. (1996). Entrainment into two-dimensional and axisymmetric turbulent gravity currents. *Journal of Fluid Mechanics*, *308*, 289–311.
- Hand, B. M. (1997). Inverse grading resulting from coarse-sediment transport lag. *Journal of Sedimentary Research*, *67*, 124–129.
- Heezen, B. C., & Ewing, W. M. (1952). Turbidity currents and submarine slumps and the 1929 Grand Banks (Newfoundland) earthquake. *American Journal of Science*, *250*, 849–873.
- Ho, V. L., Dorrell, R. M., Keevil, G. M., Burns, A. D., & McCaffrey, W. D. (2018). Pulse propagation in turbidity currents. *Sedimentology*, *65*, 620–637. <https://doi.org/10.1111/sed.12397>
- Hogg, A. J., Nasr-Azadani, M. M., & Ungarish, M. (2016). Sustained gravity currents in a channel. *Journal of Fluid Mechanics*, *798*, 853–888.
- Holyer, J. Y., & Huppert, H. E. (1980). Gravity currents entering a two-layer fluid. *Journal of Fluid Mechanics*, *100*, 739–767.
- Hsu, S., Kuo, J., Lo, C., Tsai, C., Doo, W., Ku, C., et al. (2008). Turbidity currents, submarine landslides and the 2006 Pingtung Earthquake off SW Taiwan. *Terrestrial, Atmospheric and Oceanic Sciences*, *19*, 767–772.
- Hughes, G. O. (2016). Inside the head and tail of turbulent gravity current. *Journal of Fluid Mechanics*, *790*, 1–4.
- Hughes Clarke, J. E., Brucker, S., Muggah, J., Church, I., Cartwright, D., Kuus, P., et al. (2012). *The Squamish ProDelta: Monitoring active landslide and turbidity currents. New and emerging technology* (CHC2012, 15 p.). CHC 2012, The Artic, Old Challenges New, Niagara Falls, Canada.
- Huppert, B. H. E. (1998). Quantitative modelling of granular suspension flows. *Philosophical Transactions of the Royal Society London A*, *356*, 2471–2496.
- Huppert, H. E., & Simpson, J. E. (1980). The slumping of gravity currents. *Journal of Fluid Mechanics*, *99*, 785–799.
- Islam, M. A., & Imran, J. (2010). Vertical structure of continuous release saline and turbidity currents. *Journal of Geophysical Research*, *115*, C08025. <https://doi.org/10.1029/2009JC005365>
- Ismail, H., Viparelli, E., & Imran, J. (2016). Confluence of density currents over an erodible bed. *Journal of Geophysical Research*, *121*, 1251–1272. <https://doi.org/10.1002/2015JF003768>
- Janz, G. J., & Singer, S. K. (1975). Copenhagen standard sea water: Conductivity and salinity. *Journal of Solution Chemistry*, *4*, 995–1003.
- Johnson, H. P., Gombert, J. S., Hautala, S. L., & Salmi, M. S. (2017). Sediment gravity flows triggered by remotely generated earthquake waves. *Journal of Geophysical Research: Solid Earth*, *122*, 4584–4600. <https://doi.org/10.1002/2016JB013689>
- Johnson, J. M., & Satake, K. (1994). Rupture extent of the 1938 Alaskan earthquake as inferred from tsunami waveforms. *Geophysical Research Letters*, *21*(8), 733–736.
- Kneller, B., & Buckee, C. (2000). The structure and fluid mechanics of turbidity currents: A review of some recent studies and their geological implications. *Sedimentology*, *47*, 62–94.
- Kneller, B., & McCaffrey, W. D. (2003). The interpretation of vertical sequences in turbidite beds: The influence of longitudinal flow. *Journal of Sedimentary Research*, *73*, 706–713.
- Kneller, B. C., Bennett, S. J., & McCaffrey, W. D. (1999). Velocity structure, turbulence and fluid stresses in experimental gravity currents. *Journal of Geophysical Research*, *104*(C3), 5381.
- Lambert, A., & Giovanoli, F. (1988). Records of riverborne turbidity currents and indications of slope failures in the Rhone delta of Lake Geneva. *Limnology and Oceanography*, *33*, 458–468.

- Lintern, D. G., Hill, P. R., & Stacey, C. (2016). Powerful unconfined turbidity current captured by cabled observatory on the Fraser River delta slope, British Columbia. *Sedimentology*, *63*, 1041–1064.
- Liu, J. T., Wang, Y.-H., Yang, R. J., Hsu, R. T., Kao, S. J., Lin, H. L., et al. (2012). Cyclone-induced hyperpycnal turbidity currents in a submarine canyon. *Journal of Geophysical Research*, *117*, C04033. <https://doi.org/10.1029/2011JC007630>
- Lupi, M., & Miller, S. A. (2014). Short-lived tectonic switch mechanism for long-term pulses of volcanic activity after mega-thrust earthquakes. *Solid Earth*, *5*, 13–24.
- MacVicar, B. J., Dilling, S., Lacey, R. W. J., & Hipel, K. (2014). A quality analysis of the Vectrino II instrument using a new open-source MATLAB toolbox and 2D ARMA models to detect and replace spikes. In Schleiss, A. J., de Cesare, G., Franca, M. J., & Pfister, M. (Eds.), *River flow 2014* (pp. 1951–1959). Leiden, Netherlands: CRC Press/Balkema.
- Marquardt, D. W. (1963). An algorithm for least-squares estimation of nonlinear parameters. *Journal of the Society for Industrial and Applied Mathematics*, *11*, 431–441.
- Meiburg, E., & Kneller, B. (2010). Turbidity currents and their deposits. *Annual Review of Fluid Mechanics*, *42*, 135–156.
- Mettler-Toledo (2017). *Specifications—InLab 752-6mm*. Retrieved from https://www.mt.com/gb/en/home/products/Laboratory_Analytics_Browse/pH/sensor_electrode/Conductivity_Cells/for_Bench_Meters/51344031.html
- Middleton, G. V. (1966). Experiments on density and turbidity currents II. *Canadian Journal of Earth Sciences*, *3*, 523–546.
- Middleton, G. V. (1993). Sediment deposition from turbidity currents. *Annual Review of Earth and Planetary Sciences*, *21*, 89–114.
- Mikada, H., Mitsuzawa, K., Matsumoto, H., Watanabe, T., Morita, S., Otsuka, R., et al. (2006). New discoveries in dynamics of an M8 earthquake-phenomena and their implications from the 2003 Tokachi-oki earthquake using a long term monitoring cabled observatory. *Tectonophysics*, *426*, 95–105.
- Miragliotta, G. (2011). The power of dimensional analysis in production systems design. *International Journal of Production Economics*, *131*, 175–182.
- Mulder, T., & Alexander, J. (2001). The physical character of subaqueous sedimentary density flow and their deposits. *Sedimentology*, *48*, 269–299.
- Nakajima, T., & Kanai, Y. (2000). Sedimentary features of seismoturbidites triggered by the 1983 and older historical earthquakes in the eastern margin of the Japan Sea. *Sedimentary Geology*, *135*, 1–19.
- Nelson, A. R., Briggs, R. W., Dura, T., Engelhart, S. E., Gelfenbaum, G., Bradley, L.-A., et al. (2015). Tsunami recurrence in the eastern Alaska-Aleutian arc: A Holocene stratigraphic record from Chirikof Island, Alaska. *Geosphere*, *11*, 1172–1203.
- Palanques, A., Martín, J., Puig, P., Guillén, J., Company, J. B., & Sardà, F. (2006). Evidence of sediment gravity flows induced by trawling in the Palamós (Fonera) submarine canyon (northwestern Mediterranean). *Deep-Sea Research Part I*, *53*, 201–214.
- Parker, G., Garcia, M., Fukushima, Y., & Yu, W. (1987). Experiments on turbidity currents over an erodible bed. *Journal of Hydraulic Research*, *25*, 123–147.
- Pharo, C. H., & Carmack, E. C. (1979). Sedimentation processes in short residence-time intermontane lake, Kamloops Lake, British Columbia. *Sedimentology*, *26*, 523–541.
- Piper, D. J. W., Cochonat, P., & Morrison, M. L. (1999). The sequence of events around the epicentre of the 1929 Grand Banks earthquake: Initiation of debris flows and turbidity current inferred from sidescan sonar. *Sedimentology*, *46*, 79–97.
- Piper, D. J. W., & Savoye, B. (1993). Processes of late Quaternary turbidity current flow and deposition on the Var deep-sea fan, north-west Mediterranean Sea. *Sedimentology*, *40*, 557–582.
- Piper, D. J. W., Shor, A. N., & Clarke, J. E. H. (1988). The 1929 “Grand Banks” earthquake, slump, and turbidity current. *Geological Society of America Special Paper*, *229*, 77–92.
- Sequeiros, O. E. (2012). Estimating turbidity current conditions from channel morphology: A Froude number approach. *Journal of Geophysical Research*, *117*, C04003. <https://doi.org/10.1029/2011JC007201>
- Sher, D., & Woods, A. W. (2015). Gravity currents: Entrainment, stratification and self-similarity. *Journal of Fluid Mechanics*, *784*, 130–162.
- Shin, J. O., Dalziel, S. B., & Linden, P. F. (2004). Gravity currents produced by lock exchange. *Journal of Fluid Mechanics*, *521*, 1–34.
- Simpson, J. E. (1982). Gravity currents in the laboratory, atmosphere, and ocean. *Annual Review of Fluid Mechanics*, *14*, 213–234.
- Stevenson, C. J., Talling, P. J., Wynn, R. B., Masson, D. G., Hunt, J. E., Frenz, M., et al. (2013). The flows that left no trace: Very large-volume turbidity currents that bypassed sediment through submarine channels without eroding the sea floor. *Marine and Petroleum Geology*, *41*, 186–205.
- Sumner, E. J., Siti, M. I., McNeill, L. C., Talling, P. J., Henstock, T. J., Wynn, R. B., et al. (2013). Can turbidites be used to reconstruct a paleo-earthquake record for the central Sumatran margin? *Geology*, *41*, 763–766.
- Talling, P. J., Allin, J., Armitage, D. A., Arnott, R. W., Cartigny, M. J., Clare, M. A., et al. (2015). Key future directions for research on turbidity currents and their deposits. *Journal of Sedimentary Research*, *85*, 153–169.
- Talling, P. J., Paull, C. K., & Piper, D. J. W. (2013). How are subaqueous sediment density flows triggered, what is their internal structure and how does it evolve? Direct observations from monitoring of active flows. *Earth-Science Reviews*, *125*, 244–287.
- Thomas, R. E., Schindfessel, L., McLelland, S. J., Creelle, S., & De Mulder, T. (2017). Bias in mean velocities and noise in variances and covariances measured using a multistatic acoustic profiler: The Nortek Vectrino Profiler. *Measurement Science and Technology*, *28*, 1–25.
- Umeda, M., Yokoyama, K., & Ishikawa, T. (2006). Observation and simulation of floodwater intrusion and sedimentation in the Shichikashuku reservoir. *Journal of Hydraulic Engineering*, *132*, 881–891.
- UNESCO (1983). Algorithms for computation of fundamental properties of seawater. *UNESCO Technical Papers in Marine Science*, *44*, 1–58.
- Vangriesheim, A., Khripounoff, A., & Crassous, P. (2009). Turbidity events observed in situ along the Congo submarine channel. *Deep-Sea Research Part II*, *56*, 2208–2222.
- Xu, J. P. (2010). Normalized velocity profiles of field-measured turbidity currents. *Geology*, *38*, 563–566.
- Xu, J. P. (2011). Measuring currents in submarine canyons: Technological and scientific progress in the past 30 years. *Geosphere*, *7*, 868–876.
- Xu, J. P., Noble, M. A., & Rosenfeld, L. K. (2004). In-situ measurements of velocity structure within turbidity currents. *Geophysical Research Letters*, *31*, L09311. <https://doi.org/10.1029/2004GL019718>
- Xu, J. P., Sequeiros, O. E., & Noble, M. A. (2014). Sediment concentrations, flow conditions, and downstream evolution of two turbidity currents, Monterey Canyon, USA. *Deep-Sea Research Part I*, *89*, 11–34.
- Xu, J. P., Swatzenski, P. W., Noble, M., & Li, A.-C. (2010). Event-driven sediment flux in Hueneme and Mugu submarine canyons, Southern California. *Marine Geology*, *269*, 74–88.